

Multi-Input–Multi-Output Control of a Utility-Scale, Shaftless Energy Storage Flywheel With a Five-Degrees-of-Freedom Combination Magnetic Bearing

Xiaojun Li

Mem. ASME
Department of Mechanical Engineering,
Texas A&M University,
College Station, TX 77840
Motion Control Group,
Rockwell Automation,
Minneapolis, MN 55344
e-mail: Tonylee2016@gmail.com

Alan Palazzolo

Fellow ASME
Department of Mechanical Engineering,
Texas A&M University,
College Station, TX 77840
e-mail: a-palazzolo@tamu.edu

The modeling and control of a recently developed utility-scale, shaftless, hubless, high strength steel energy storage flywheel system (SHFES) are presented. The novel flywheel is designed with an energy/power capability of 100 kWh/100 kW and has the potential of a doubled energy density when compared to conventional technologies. In addition, it includes a unique combination magnetic bearing (CAMB) capable of providing five-degrees-of-freedom (5DOF) magnetic levitation. Initial test results show that the CAMB, which weighs 544 kg, can provide a stable lift-up and levitation control for the 5543 kg flywheel. The object of this paper is to formulate and synthesize a detailed model as well as to design and simulate a closed-loop control system for the proposed flywheel system. To this end, the CAMB supporting structures are considered flexible and modeled by finite element modeling. The magnetic bearing is characterized experimentally by static and frequency-dependent coefficients, the latter of which are caused by eddy current effects and presents a challenge to the levitation control. Sensor-runout disturbances are also measured and included. System nonlinearities in power amplifiers and the controller are considered as well. Even though the flywheel has a large ratio of the primary-to-transversal moment of inertias, multi-input–multi-output (MIMO) feedback control demonstrates its effectiveness in canceling gyroscopic torques at the designed operational spinning speed. Various stages of proportional and derivative (PD) controllers, lead/lag compensators, and notch filters are implemented to suppress the high-frequency sensor disturbances, structural vibrations, and rotor imbalance effects.

[DOI: 10.1115/1.4039857]

Keywords: magnetic levitation, Maglev, multi-input–multi-output control (MIMO), active magnetic bearing (AMB), shaftless energy storage flywheel (SHFES), battery, renewable energy

1 Introduction

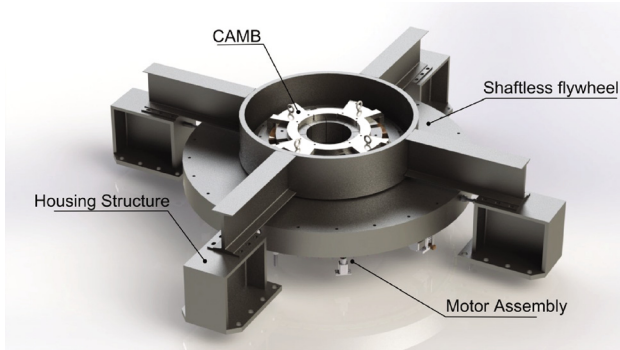
Flywheel energy storage systems (FESS) provide solutions for both energy storage and distribution. Compared to electrochemical batteries, they have high power ratings, superior depth of discharge and lifetime charge cycles [1]. FESSs are ideal for power grid regulations since they can improve the distribution efficiency, as well as smooth power output from renewable energy sources such as wind or solar farms. Through a motor/generator, energy is stored in a flywheel in the form of rotating kinetics. The same electrical machine allows the stored energy to be discharged back to electricity. Apart from frequency regulation and renewable energy, typical applications of a FESS also include uninterruptible power service, hybrid locomotives, and so on. For a FESS, the flywheel is usually supported by an active magnetic bearing (AMB) system to avoid any friction loss or wear caused by conventional bearings. Also, its performance can be conveniently adjusted by tuning the feedback control parameters. Conventional AMB systems often require three different actuators, which would be in the form of two radial and one axial device, to provide a five-degrees-of-freedom (5DOF) levitation control.

The research on energy storage flywheel has focused on different aspects. Talebi and coworkers [2] discussed the schemes to

design power electronics and controllers such that the FESS has increased power output. The primary target was to increase the discharge power up to four times to the nominal rating of the PMSM. Sung et al. [3] developed a 300 Wh flywheel supported by two super-conducting Magnetic Bearing. The superconducting magnetic bearing does not need active control and was capable of achieving 20,000 rpm spin speed. Jinji et al. [4] proposed a novel integrated radial hybrid magnetic bearing for small-sized magnetically suspended control moment gyroscope. The magnetic bearing can control four degrees-of-freedom of motions. Magnetic bearing control is instrumental and often directly related to flywheel applications. Park et al. [5] studied the multi-input–multi-output (MIMO) control of a magnetically levitated FESS and showed its benefit comparing to a single-input–single output (SISO) control scheme. Lei and Palazzolo [6] studied the control of AMBs for a large order, flexible shaft which is modeled by finite element model (FEM). As discussed in Ref. [7], an optimal state feedback controller is used for stabilizing an AMB-supported flexible rotor. Lei et al. [8] also designed a nonlinear fuzzy logic-based controller for an AMB supported flexible shaft. Wang [9,10] presented the initial design and use of shaftless flywheel for railroad applications, to reduce trains' NO_x emissions and fuel consumptions. A flux-weakening control scheme is also proposed to improve the regenerating efficiency.

The newly developed and built FESS, which features a patented, shaftless, hubless, and high strength steel flywheel [11–13], will be referred to as shaftless, hubless, high strength

Contributed by the Dynamic Systems Division of ASME for publication in the JOURNAL OF DYNAMIC SYSTEMS, MEASUREMENT, AND CONTROL. Manuscript received September 14, 2017; final manuscript received March 24, 2018; published online May 7, 2018. Assoc. Editor: Davide Spinello.



(a)



(b)

Fig. 1 The SHFES flywheel with rated energy and power of 100Kwh/100 KW: (a) three-dimensional drawing of the SHFES with system components illustrated and (b) the newly built, full-scale SHFES

steel flywheel energy storage system (SHFES) in the remainder of this paper. The shaftless flywheel is an extension and physical realization of the concept presented in Refs. [11] and [13]. Novel designs give the SHFES a potential of doubled energy density. Along with the use of low-cost materials, it provides a competitive alternative to lion-batteries regarding both costs and availability. Nevertheless, the use of new technologies, such as the large-scale and high-inertia flywheel, combination magnetic bearing (CAMB) with solid cores, poses challenges for the levitation control, flywheel stability, and disturbance rejection at full speed. The magnetic bearing control is also made complicated by the presence of precession and nutation poles that result from gyroscopic moments of the spinning flywheel [5]. The object of this research is to formulate and synthesize a detailed model that includes a flexible support structure, frequency-dependent magnetic bearing responses, sensory disturbances, and nonlinearity effects. Based on the model, a feedback control, which features MIMO cross-feedback terms, are designed to cancel the gyroscopic moments and to provide stable flywheel levitation control during the initial lift-up and high-speed spinning. It is critical that the power amplifiers that drive the CAMB are not working under high saturations. Small voltage and current variations of the coils are also desirable for minimizing AMB power loss. The controller employed also includes direct proportional and derivative (PD) gains, lead/lag compensators and notch filters for suppressing sensor runout, imbalance, and mechanical resonances.

2 Overview of Shaftless, Hubless, High Strength Steel Flywheel Energy Storage System

The SHFES, which includes the shaftless flywheel, CAMB, and motor/generator is depicted in Fig. 1. Unlike many existing flywheel technologies that use composite materials, it adopts high strength steel (AISI 4340) as the building material. High strength

Table 1 Flywheel specifications

Parameter name	Quantity	Unit
Flywheel outer diameter	2133	(mm)
Flywheel height	20	(mm)
Flywheel mass	5443	(kg)
Moment of inertia	3087	(kg·m ²)
Rotational speed	5000	(rpm)
Tip speed	558	(m/s)
Energy/power capacity	100/100	(kWh/kW)
Materials	4340	AISI
Material tensile strength	1500	(MPa)
Flywheel relative magnetic permeability	200	—

steel cost much lower than composite per material strength.¹ The manufacture and fabrications, as well as recycling, are also made easy with the composite components being replaced. Moreover, SHFES has predictable fatigue life cycles and are designed to last for 30 years of operation. As shown in the core component of the SHFES is a shaftless, hubless high strength steel flywheel weighing 5443 kg. The design is entirely different from a conventional flywheel, which has a shaft and hole through its center.

The specific energy E of a flywheel is proportional to its yield strength σ and shape factor K . The SHFES is in the form of a solid disk and has a shape factor that is almost two times higher than an annulus flywheel [12,14]

$$E = K\sigma$$

$$K \approx 0.6 \text{ for the SHFES} \quad (1)$$

$$K \approx 0.3 \text{ for annulus flywheels}$$

On top of the flywheel lies a single combination CAMB, which is supported by a housing structure. The nominal air gap between the CAMB and the flywheel is between 1.02 mm and 1.14 mm. A touch-down bearing system is installed underneath the flywheel for drop protection in case of AMB failures. Coreless Permanent-magnets motor/generators are designed for the SHFES. The torque, power, current, and speed of the electrical machine are determined by finite element electromagnetic analysis to meet the design requirement [15]. The flywheel is also designed to work in a vacuum chamber to eliminate windage losses. Table 1 summarizes the main specifications of the SHFES.

3 Modeling of the Shaftless, Hubless, High Strength Steel Flywheel Energy Storage System

The entire electromechanical system includes following components:

- Magnetic bearing with eddy current effects.
- Flywheel with gyroscopic effects.
- Flexible Housing structure.
- Sensor dynamics.
- Power amplifiers with saturation effects and coil inductance/resistance.
- Feedback controller with SISO and MIMO control algorithms.

3.1 Modeling of the Combo-Active Magnetic Bearing. To include the CAMB into system dynamic simulation. It is characterized by static and frequency-dependent coefficients. Static characteristics of the CAMB include position and current stiffness (shown in Table 2). Studies are carried out near the equilibrium position where the flywheel is horizontally centered and placed 1.016 mm (40 mils) below the CAMB vertically. At the equilibrium position, current stiffness is acquired by giving current excitations at different amperages to the radial, axial, and tilting coils, respectively. Similarly, position stiffness is obtained by measuring the magnetic forces when different position/attitude is applied to the flywheel, with the current electromagnetic force excluded.

¹<http://www.energy.ca.gov/>

Table 2 The measured current and position stiffness of the CAMB

	Axial	Radial	Tilting
K_p	-2.599×10^7 (N/m)	-1.858×10^6 (N/m)	-2.737×10^6 (N·m/rads)
K_i	3714 (N/A)	320 (N/A)	546 (N·m/A)
Coil turns	200	100	100

Because that there are both radial and axial flux paths (Fig. 2) in the CAMB, the conventional laminated design is difficult to apply. It is not cost-effective either. For nonlaminated design, eddy current effect is ineligious. This phenomenon causes amplitude attenuation and phase lag in electromagnetic force as the excitation frequency increases. Since the magnetic bearing affects system dynamics considerably, accurate modeling is beneficial for both design and simulation. The magnetic attraction force can be derived from the virtual work principle

$$f = \frac{1}{2\mu_0} \oint (B_{pm} + B_i)^2 dA \quad (2)$$

Since the AMB is also designed to work in a linear range, the linearized magnetic force with respect to the flux density B_i is

$$f = \frac{B_{pm}}{\mu_0} \oint B_i dA \quad (3)$$

The frequency response of force to current can be then approximated by the frequency response of flux ($\phi_i(\omega)$) to current $I(\omega)$ or the average flux density ($\bar{B}_i(\omega)$) to current [16]

$$\frac{f(\omega)}{f(0)} \approx \frac{\oint B_i(I(\omega)) dA}{\oint B_i(I(0)) dA} = \frac{\Phi(I(\omega))}{\Phi(I(0))} = \frac{\bar{B}_i(I(\omega))}{\bar{B}_i(I(0))} \quad (4)$$

For the CAMB, the axial and tilt AMB flux to current responses, which are essential for controlling the gyroscopic effects and crucial to the flywheel's stability, are accessible for measurement with the present instrument (depicted in Fig. 3).

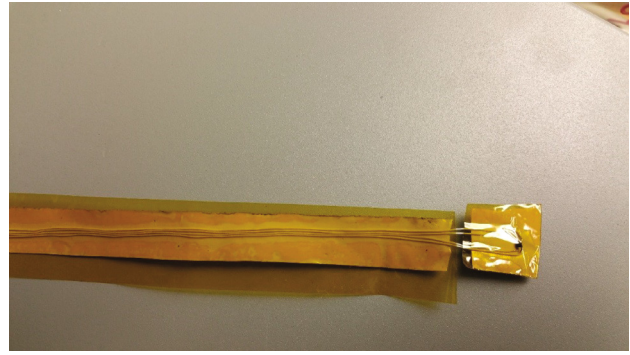


Fig. 3 In-house magnetic field density measurement tool

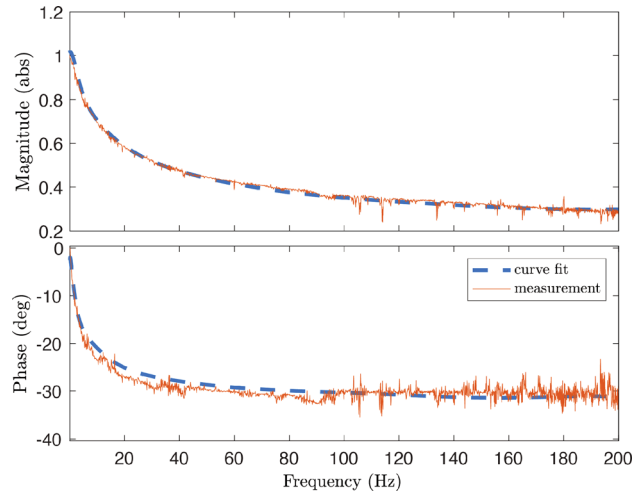


Fig. 4 Curve fitting for CAMB frequency response: tilt actuator

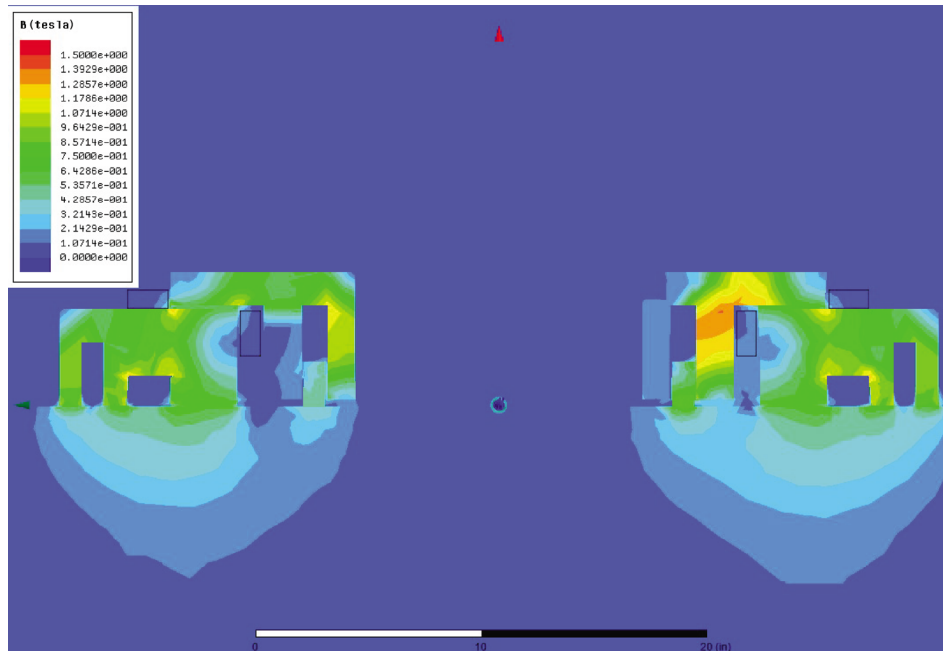


Fig. 2 Section flux plot of three-dimensional electromagnetic static simulation

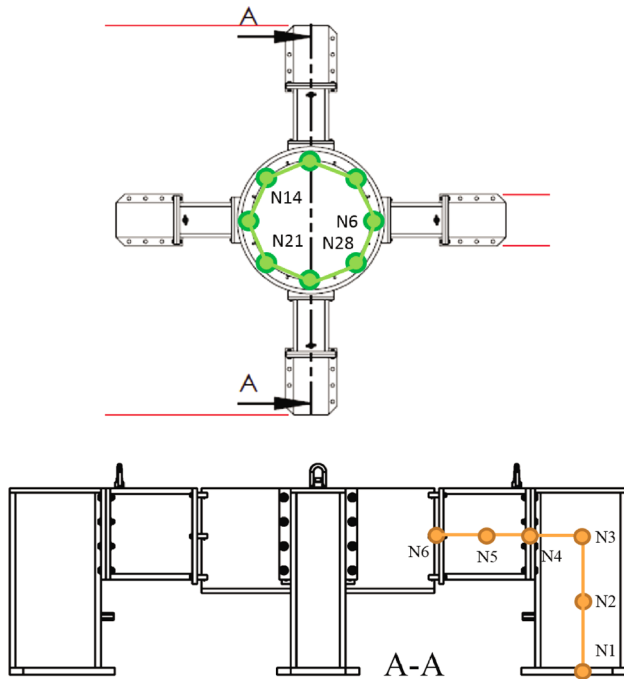


Fig. 5 Housing structure nodes and beam elements

The frequency response can be described by a fractional-order model, which is difficult to be included in dynamical simulations. Therefore, the results are curve-fitted [17] as transfer functions and incorporated into the later system modeling. As depicted in Fig. 4, for the tilting actuator of the CAMB, the magnitude attenuation and the phase lag at 60 Hz are close to 40% and 30 deg.

In summary, the magnetic force generated by the CAMB synthesized by position and current-related coefficients are

$$f_{em} = K_p(q_s^* - q_f) + TF_{if}K_i I \quad (5)$$

where q_s^* is the displacement vector of the stator nodes where the CAMB is installed, q_f is the displacement vector of the flywheel, and $TF_{if}K_i I$ is the current-induced magnetic force term with K_i being the static current stiffness matrix, TF_{if} being the transfer function matrix, and I being the excitation current vector. Aforementioned, the transfer functions are curve-fitted as the below equation:

$$TF_i(j) = \frac{\sum_{i=0}^N a_i s^{N-i}}{\sum_{i=0}^M b_i s^{M-i}} \quad (6)$$

3.2 Modeling of the Flexible Support Structure. The shaftless design eliminates the flexible shaft modes. Nevertheless, the CAMB is supported by a housing structure which plays a vital role in system dynamics. A beam-element FEM model is used for modeling the support structure and AMB (together will be referred as the stator). The structure dynamics are given by the following equation:

$$M_s \ddot{q}_s + C_s \dot{q}_s + K_s q_s = -f_{em} \quad (7)$$

In which M_s and K_s are the stator's mass and stiffness matrices. q_s is stator's displacement vector defined by the equation given below:

$$q_s = [\theta_{x,1}, \theta_{y,1}, x_1, y_1, z_1, \dots, \theta_{x,n}, \theta_{y,n}, x_n, y_n, z_n]^T \quad (8)$$

where n is the number of free nodes. The C_s matrix is the proportional damping based on:

$$C_s = aM_s + bK_s \quad (9)$$

The coefficients are obtained by assuming normalized 2% damping at 60 Hz and 1% damping at 100 Hz. The finite element model of the stator includes 28 nodes and 144 DOF. As depicted in Fig. 5, different types of beam elements are used. The elements shown in the top view are solid beams arranged in an octagon shape for approximating the circle thin wall component in the housing structure. The reaction force from the flywheel is applied to the these nodes. The elements shown in the section view are I-beams for modeling the rest part of the structure. The 28-node-FEM model gives similar natural frequency results compared to the solid modeling but requires much less computation effort. Figure 6 shows the FEM model (along with an axial mode shape) in MATLAB. To include the AMB, it is modeled by shell elements bounded by the green nodes. The shell elements bring extra displacements and bending stiffness in addition to the thin wall elements (Table 3).

The force/moment distribution matrix D_f , which converts the magnetic forces from the flywheel's coordinate to the coordinate of the stator, is defined by the following equations:

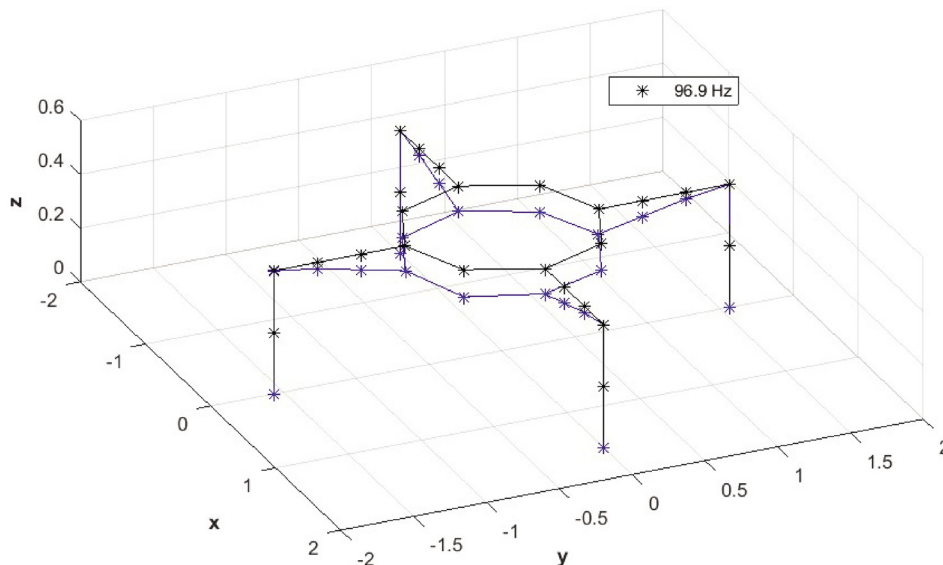


Fig. 6 Housing structure model in MATLAB, showing a vertical mode

$$f_{em}^{st}(i) = D_f(i) \begin{bmatrix} M_{\theta_x} \\ M_{\theta_y} \\ f_x \\ f_y \\ f_z \end{bmatrix} \quad (10)$$

$$D_f(6) = \begin{bmatrix} 0 & 0 & \frac{1}{8} & 0 & 0 \\ 0 & 0 & 0 & \frac{1}{8} & 0 \\ 0 & -m2f & 0 & 0 & \frac{1}{8} \\ 0 & \dots & 0 & & \\ \vdots & \ddots & \vdots & & \\ 0 & \dots & 0 & & \end{bmatrix}, \quad D_f(7) = \begin{bmatrix} 0 & 0 & \frac{1}{8} & 0 & 0 \\ 0 & 0 & 0 & \frac{1}{8} & 0 \\ m2f & -m2f & 0 & 0 & \frac{1}{8} \\ 0 & \dots & 0 & & \\ \vdots & \ddots & \vdots & & \\ 0 & \dots & 0 & & \end{bmatrix}, \quad D_f(8) = \begin{bmatrix} 0 & 0 & \frac{1}{8} & 0 & 0 \\ 0 & 0 & 0 & \frac{1}{8} & 0 \\ m2f & 0 & 0 & 0 & \frac{1}{8} \\ 0 & \dots & 0 & & \\ \vdots & \ddots & \vdots & & \\ 0 & \dots & 0 & & \end{bmatrix}$$

$$D_f(14) = 0 \begin{bmatrix} 0 & 0 & \frac{1}{8} & 0 & 0 \\ 0 & 0 & 0 & \frac{1}{8} & 0 \\ m2f & m2f & 0 & 0 & \frac{1}{8} \\ 0 & \dots & 0 & & \\ \vdots & \ddots & \vdots & & \\ 0 & \dots & 0 & & \end{bmatrix}, \quad D_f(15) = \begin{bmatrix} 0 & 0 & \frac{1}{8} & 0 & 0 \\ 0 & 0 & 0 & \frac{1}{8} & 0 \\ 0 & m2f & 0 & 0 & \frac{1}{8} \\ 0 & \dots & 0 & & \\ \vdots & \ddots & \vdots & & \\ 0 & \dots & 0 & & \end{bmatrix} \quad (11)$$

$$D_f(21) = \begin{bmatrix} 0 & 0 & \frac{1}{8} & 0 & 0 \\ 0 & 0 & 0 & \frac{1}{8} & 0 \\ -m2f & m2f & 0 & 0 & \frac{1}{8} \\ 0 & \dots & 0 & & \\ \vdots & \ddots & \vdots & & \\ 0 & \dots & 0 & & \end{bmatrix}, \quad D_f(22) = \begin{bmatrix} 0 & 0 & \frac{1}{8} & 0 & 0 \\ 0 & 0 & 0 & \frac{1}{8} & 0 \\ -m2f & 0 & 0 & 0 & \frac{1}{8} \\ 0 & \dots & 0 & & \\ \vdots & \ddots & \vdots & & \\ 0 & \dots & 0 & & \end{bmatrix}, \quad D_f(28) = \begin{bmatrix} 0 & 0 & \frac{1}{8} & 0 & 0 \\ 0 & 0 & 0 & \frac{1}{8} & 0 \\ -m2f & -m2f & 0 & 0 & \frac{1}{8} \\ 0 & \dots & 0 & & \\ \vdots & \ddots & \vdots & & \\ 0 & \dots & 0 & & \end{bmatrix}$$

where $m2f = -1/((\sqrt{2} + 1)D_s)$ is the factor that convert the flywheel(moment to node magnetic forces. The sensor collection matrices, which collects the position sensor data in the stator's coordinate and convert them to the CAMB's coordinate, is defined by Eqs. (12) and (13). Sensitivity measurements are summarized in Table 4

$$q_s^c = \begin{bmatrix} \theta_x \\ \theta_y \\ x \\ y \\ z \end{bmatrix} = \sum D_s(i)q_s(i) \quad (12)$$

Table 3 Reaction and sensor allocation on housing nodes

	Fraction	Radial		Axial	Moment	
		X	Y	Z	M_{θ_x}	M_{θ_y}
Reaction force nodes	1/8	N6, N15, N8, N22 N7, N14, N21, N28		N6-8, N14-15, N21-22, N28	N7 N8 N14 N21 N22 N28	N14 N15 N21, N6 N7 N28
Sensor nodes	—	N6, N15	N8, N22	N6, N15, N8, N22	N8, N22	N15, N6

$$\begin{aligned}
\mathbf{D}_s(6) &= \begin{bmatrix} 0 & 0 & 0 & 0 & 0 & 0 \\ 0 & 0 & \frac{1}{D_s} & 0 & 0 & 0 \\ \frac{1}{8} & 0 & 0 & 0 & 0 & 0 \\ 0 & \frac{1}{8} & 0 & 0 & 0 & 0 \\ 0 & 0 & \frac{1}{8} & 0 & 0 & 0 \end{bmatrix}, & \mathbf{D}_s(7) &= \begin{bmatrix} 0 & 0 & 0 & 0 & 0 & 0 \\ 0 & 0 & 0 & 0 & 0 & 0 \\ \frac{1}{8} & 0 & 0 & 0 & 0 & 0 \\ 0 & \frac{1}{8} & 0 & 0 & 0 & 0 \\ 0 & 0 & \frac{1}{8} & 0 & 0 & 0 \end{bmatrix}, & \mathbf{D}_s(8) &= \begin{bmatrix} 0 & 0 & \frac{1}{D_s} & 0 & 0 & 0 \\ 0 & 0 & 0 & 0 & 0 & 0 \\ \frac{1}{8} & 0 & 0 & 0 & 0 & 0 \\ 0 & \frac{1}{8} & 0 & 0 & 0 & 0 \\ 0 & 0 & \frac{1}{8} & 0 & 0 & 0 \end{bmatrix} \\
\mathbf{D}_s(14) &= \begin{bmatrix} 0 & 0 & 0 & 0 & 0 & 0 \\ 0 & 0 & 0 & 0 & 0 & 0 \\ \frac{1}{8} & 0 & 0 & 0 & 0 & 0 \\ 0 & \frac{1}{8} & 0 & 0 & 0 & 0 \\ 0 & 0 & \frac{1}{8} & 0 & 0 & 0 \end{bmatrix}, & \mathbf{D}_s(15) &= \begin{bmatrix} 0 & 0 & 0 & 0 & 0 & 0 \\ 0 & 0 & -\frac{1}{D_s} & 0 & 0 & 0 \\ \frac{1}{8} & 0 & 0 & 0 & 0 & 0 \\ 0 & \frac{1}{8} & 0 & 0 & 0 & 0 \\ 0 & 0 & \frac{1}{8} & 0 & 0 & 0 \end{bmatrix} \\
\mathbf{D}_s(21) &= \begin{bmatrix} 0 & 0 & 0 & 0 & 0 & 0 \\ 0 & 0 & 0 & 0 & 0 & 0 \\ \frac{1}{8} & 0 & 0 & 0 & 0 & 0 \\ 0 & \frac{1}{8} & 0 & 0 & 0 & 0 \\ 0 & 0 & \frac{1}{8} & 0 & 0 & 0 \end{bmatrix}, & \mathbf{D}_s(22) &= \begin{bmatrix} 0 & 0 & -\frac{1}{D_s} & 0 & 0 & 0 \\ 0 & 0 & 0 & 0 & 0 & 0 \\ \frac{1}{8} & 0 & 0 & 0 & 0 & 0 \\ 0 & \frac{1}{8} & 0 & 0 & 0 & 0 \\ 0 & 0 & \frac{1}{8} & 0 & 0 & 0 \end{bmatrix}, & \mathbf{D}_s(22) &= \begin{bmatrix} 0 & 0 & 0 & 0 & 0 & 0 \\ 0 & 0 & 0 & 0 & 0 & 0 \\ \frac{1}{8} & 0 & 0 & 0 & 0 & 0 \\ 0 & \frac{1}{8} & 0 & 0 & 0 & 0 \\ 0 & 0 & \frac{1}{8} & 0 & 0 & 0 \end{bmatrix}
\end{aligned} \tag{13}$$

The flywheel's equation of motion is given by Eq. (14):

$$\mathbf{M}_f \ddot{\mathbf{q}}_f + \mathbf{G}_f(\omega) \dot{\mathbf{q}}_f = \mathbf{f}_{em} + \mathbf{f}_{im} \tag{14}$$

in which $\mathbf{q}_f = [\theta_{x,f}, \theta_{y,f}, x_f, y_f, z_f]^T$ denotes the flywheel position vector. The Imbalance force is defined as $\mathbf{f}_{im} = [0, 0, me\omega^2 \cos t(\omega t), me\omega^2 \sin(\omega t), 0]^T$. $\mathbf{G}_f(\omega)$ denotes the speed dependent gyroscopic matrix

$$\mathbf{G}_f = \begin{bmatrix} 0 & I_p \omega & 0 & 0 & 0 \\ -I_p \omega & 0 & 0 & 0 & 0 \\ 0 & 0 & 0 & 0 & 0 \\ 0 & 0 & 0 & 0 & 0 \\ 0 & 0 & 0 & 0 & 0 \end{bmatrix} \tag{15}$$

3.3 Modeling of Power Amplifier and Coil. Power amplifiers are modeled as simple proportional feedback systems that include coil inductance and resistance. The governing equation of the power amplifiers is given in the following:

$$\mathbf{V} = \mathbf{K}_{PA}(\mathbf{G}_{PA}\mathbf{v} - \mathbf{i}) = \mathbf{L} \frac{d\mathbf{i}}{dt} + \mathbf{R}\mathbf{i} \tag{16}$$

where \mathbf{K}_{PA} denotes the feedback gain matrix, and \mathbf{G}_{PA} denotes the sensitivity matrix for the power amplifiers, respectively. The amplifier voltage and current are limited to maximum thresholds

$$-\mathbf{V}_{\lim} < \mathbf{V} < \mathbf{V}_{\lim} \tag{17}$$

Active magnetic bearing coil inductances have substantial effects on the power amplifier bandwidth. To accurately estimate the

flywheel's dynamics, inductances are measured experimentally by exciting each coil with sinusoidal voltages and recording their current responses

$$\frac{I}{V} = \frac{1}{Lj\omega + R} \tag{18}$$

The impedance can be decomposed into the inductance and resistance parts. While more sophisticated models take the frequency dependence of R and L into account [18]. Here, the measurements were carried out at the nominal airgaps, and the inductances and resistance are derived around the operational frequency (5000 rpm).

3.4 Modeling of Sensors Dynamics and Disturbances.

Proximity sensors are typically used in AMB suspension control. In general, these sensors have a relatively high bandwidth of near to 10 kHz. The sensor dynamics are summarized as follows:

$$\mathbf{u} = \frac{\mathbf{G}_{sn}}{(\mathbf{T}_{sn}s + 1)} (\mathbf{q}_s - \mathbf{q}_f + \mathbf{q}_r) \tag{19}$$

where \mathbf{q}_s and \mathbf{q}_f are the stator and flywheel position vectors in the CAMB's coordinate. \mathbf{G}_{sn} and \mathbf{T}_{sn} are the sensitivity and filter time

Table 4 Comparison of natural frequency between MATLAB code and ANSYS simulation results

Source	Axial (Hz)	Moment (Hz)
Beam FEMUsed for MATLAB simulation	96.7	192
Solid FEM	102	165

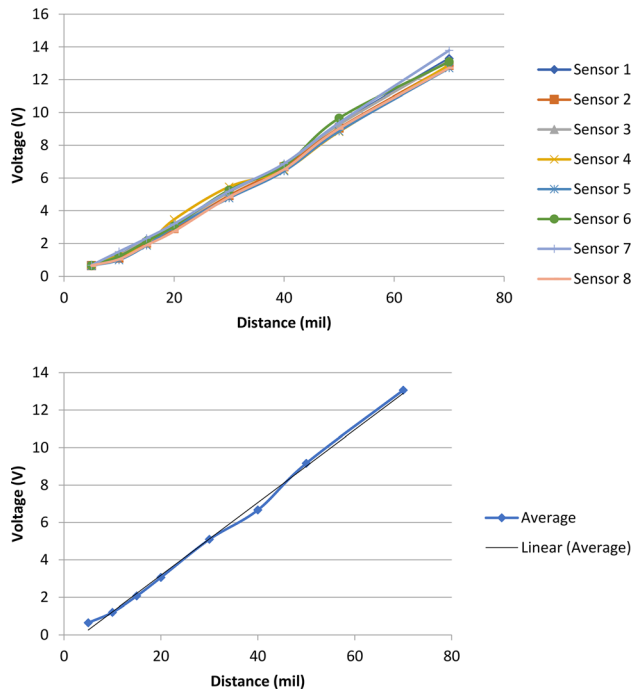


Fig. 7 Sensitivity measurements and linear regression of the proximity sensors

matrices. As depicted in Fig. 7, the average sensitivity is about 7.362 v/mm (178 mv/mil).

The q_r vector denotes the sensor runout components. As defined in Eq. (20), they are modeled as a synthesis of sinusoidal signals that are dependent of the running speed

$$q_r = \sum_{i=1}^N A_n \sin(f_n \omega t) + B_n \cos(f_n \omega t) \quad (20)$$

Notice that, apart from the surface flatness of the flywheel, vertical or horizontal misalignments between the flywheel and the stator may also contribute to the runouts. The entire closed-loop system is illustrated in Fig. 8.

4 Controller Design

4.1 Multiple-Input-Multiple-Output Control. Since the flywheel is very close to the form of a thin disk, the I_p to I_t ratio

of it is almost 2, which leads to a strong gyroscopic effect. The gyroscopic effect generates pairs of forward and backward conical modes. As the spin speed increases, the rigid body forward mode converges to a linear slope of the spin speed ($\omega I_p / I_t$) as the backward one converges to zero. Gyroscopic effect alone only pulls the poles to the imaginary axis, which causes the system to be marginally stable. However, with certain phase lags from the AMB, amplifiers, or other parts of the system, these modes will become unstable. While a SISO control algorithm will levitate the flywheel, it is not able to stabilize the system when the flywheel is rotating at high-speed. MIMO algorithm [5,19,20] is applied to cancel some of the gyroscopic moment effects. The controller also features a PD stage, multiple lead-lag filters, and multiple notch filters. The main task of the control algorithm is to stabilize the flywheel and prevent the power amplifier, digital controller, and magnetic bearing from being working under saturated conditions. The rotor imbalance and sensor runout signals can be viewed as running speed-dependent disturbances in the system with the imbalance being applied to the flywheel and runout signals applied to the sensors. In particular, high-frequency harmonic components of the sensor runout signals will be magnified by derivative feedback, causing a great burden on the power amplifiers. Multiple notch filter stages are designed for each channel to suppress the sensor runout disturbances.

In summary, the overall control algorithm for 5DOF is summarized by the following equation:

$$v = \left(P + D \frac{s}{s + \tau} \right) [L_l L_g N_f] T_{u2v} (u - u^T) \quad (21)$$

The proportional gain matrix is defined as in the equation given below:

$$P = \begin{bmatrix} P_x & & & & \\ & P_y & & & \\ & & P_{\theta x} & P_{\theta c} & \\ & & -P_{\theta c} & P_{\theta y} & \\ & & & & P_z \end{bmatrix} \quad (22)$$

Moreover, the derivative matrix is defined in the below equation:

$$D = \begin{bmatrix} D_x & & & & \\ & D_y & & & \\ & & D_{\theta x} & -D_{\theta c} & \\ & & D_{\theta c} & D_{\theta y} & \\ & & & & D_z \end{bmatrix} \quad (23)$$

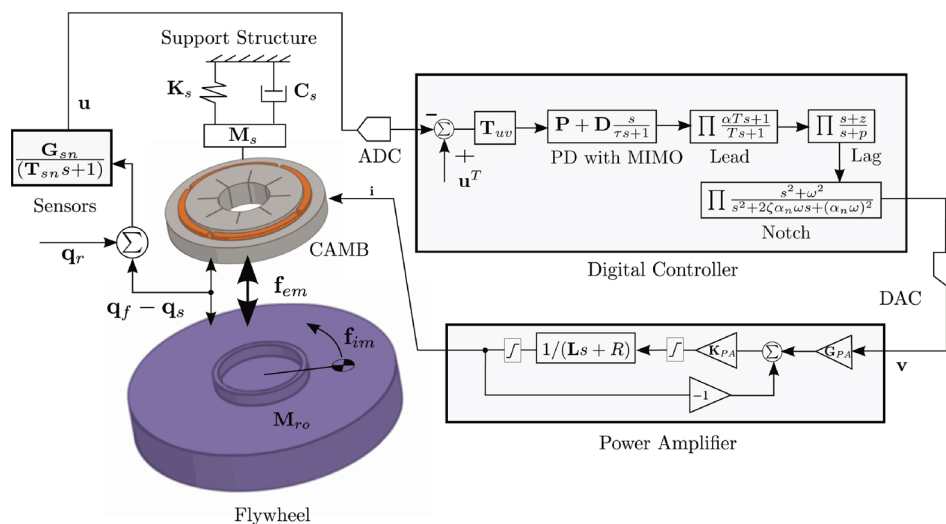


Fig. 8 Flywheel dynamics simulation schematic

where P_{0c} and D_{0c} are the cross-couple proportional and damping coefficients. In the effort of weakening the gyroscopic effects, the cross-coupled feedback applies torque in one plane per the angular position and velocity in its quadrature plane. This strategy reduces the speed dependency of system dynamics (conical modes) and lowers the frequency of forward modes so that derivate gains can be more effective [5].

4.2 Compensators and Filters. In addition to the PD regulators and lag compensators, each feedback channel also includes various lead compensators and notch filters. The lead compensators provide finite bandwidth derivatives for a specific range of frequencies so that the system's stability and response can be improved. The transfer function used for the lead compensator is defined in the following equation:

$$L_l = \prod_{i=1}^N \text{diag}_i \left(\frac{\alpha(1)T(1)s + 1}{T(1)s + 1} \quad \dots \quad \frac{\alpha(5)T(5)s + 1}{T(5)s + 1} \right)$$

(lead stages)

where $\alpha(i) = \frac{1 + \sin(\phi_i)}{1 - \sin(\phi_i)}$ and $T(i) = \frac{1}{\omega_c(i)\sqrt{\alpha(i)}}$

(24)

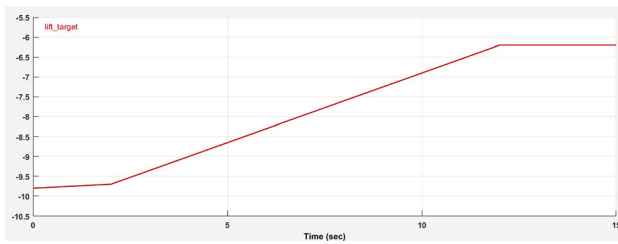


Fig. 9 Axial target profile

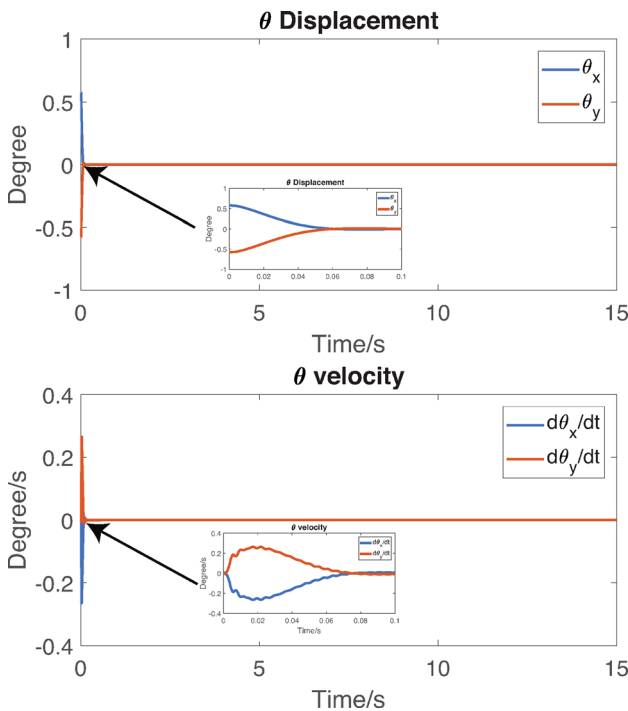


Fig. 10 Flywheel attitudes during lift-up

In which $\phi(i)$ and $\omega_c(i)$ denote the maximum phase and the center frequencies, respectively. The notch filters are critical in suppressing vibration resonances. They are also instrumental in canceling high-frequency structural modes and suppressing sensor runouts, which would be amplified by derivative feedback. If left attended, these sensor runouts could lead to amplifier saturations and instabilities. The transfer functions of notches filters are given by the following equations:

$$N = \prod_{k=1}^Q \text{diag}_k \left(\frac{s^2 + \omega^2(1)}{s^2 + 2\zeta(1)\beta_n(1)\omega(1) + (\beta_n(1)\omega(1))^2}, \dots, \frac{s^2 + \omega^2(5)}{s^2 + 2\zeta(5)\beta_n(5)\omega(5) + (\beta_n(5)\omega(5))^2} \right) \text{ (notch stages)} \quad (25)$$

where ζ_i determines the rejection bandwidth and depth. $\omega_i(n)$ is the notch frequency, and β_i decides the pole position offset. The lag compensator's transfer functions are defined in the following equation:

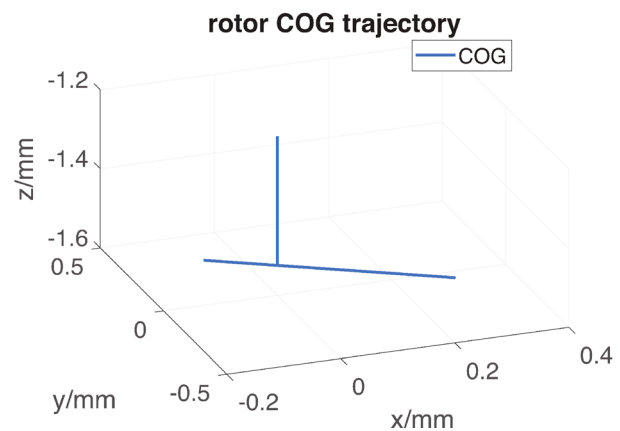
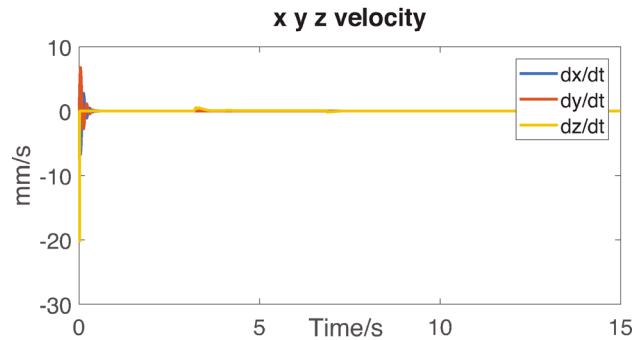
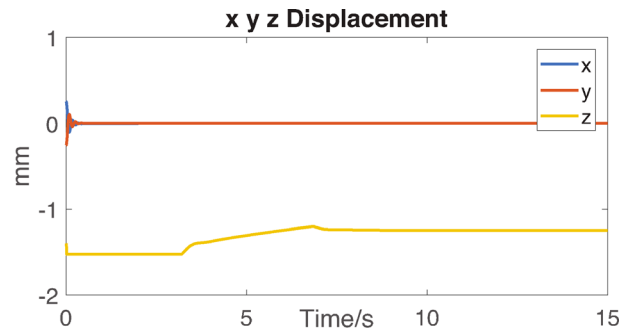


Fig. 11 Flywheel trajectory during lift-up

$$L_g = \prod_{j=1}^M \text{diag}_j \left(\frac{s+z(1)}{s+p(1)} \quad \dots \quad \frac{s+z(5)}{s+p(5)} \right) \text{ (lag stages)} \quad (26)$$

5 Simulation

A Simulation platform is developed for the SHFES in MATLAB/SIMULINK. Motor dynamics are not included in the simulation model since it has minimal effects on the magnetic levitation, the flywheel is assumed to be ideally speed controlled by the brushless direct current motor.

5.1 Simulation of the Levitation Process. During the levitation process, the axial target is set to be raised slowly to the equilibrium position to avoid excessive overshoot (Figs. 9–11). A slower lag filter is given to the axial controller so that the flywheel will achieve the radial target at first. This technique facilitates the later axial levitation. One notch per channel is used for each of the radial controllers during lift-up. Two notches are used for the remaining channels. The axial control target must be gradually raised to 1.143 mm (40 mils) to prevent delevitation resulted by overshoot. Because of this approach, the actual rotor will stay on the catcher bearing for several seconds after the controller is turned on. This increases the demand on the axial amplifier (illustrated in Fig. 12). However, the demand quickly diminishes when the rotor loses contact with the catcher bearings. The radial actuator has the least problems during both lift-up and steady-state due to their lesser inductances. As depicted in Fig. 13, the axial force generated by current excitation gradually increases when the lag compensator is engaged. When it reaches the maximum value, the flywheel leaves the catcher bearing. In the meantime, the stator was pulled down by 0.13 mm (5 mils) as shown in Fig. 14. After the flywheel reaches the equilibrium position, the current generated magnetic force is close to zero.

5.2 Simulation of Flywheel at Full Speed. The following simulation is carried out when the flywheel is operating at the rated

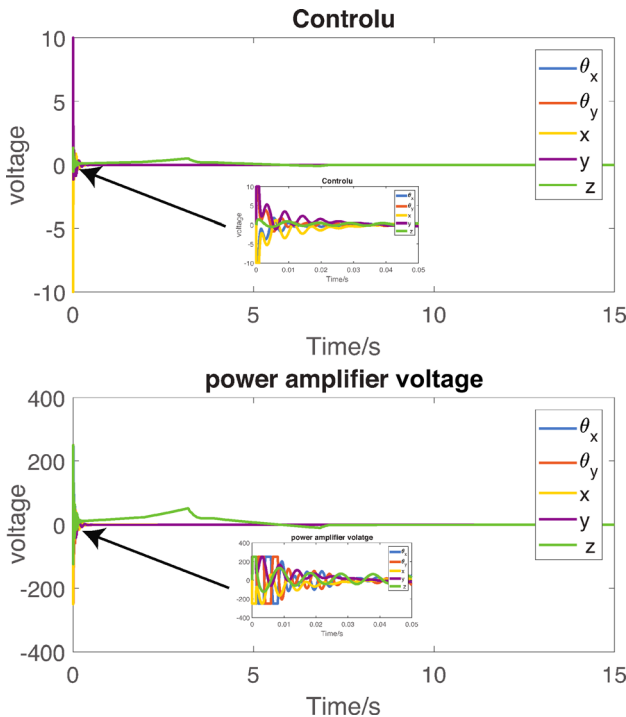


Fig. 12 Controller output and power amplifier voltage during lift-up

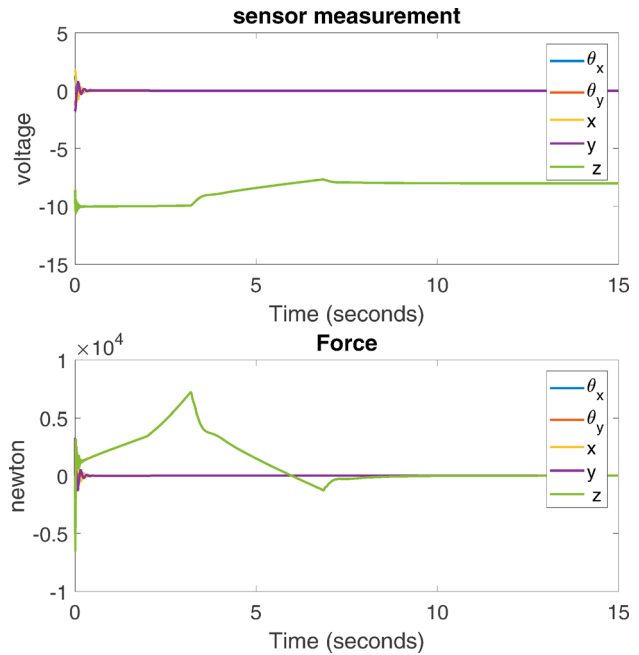


Fig. 13 Sensor and magnetic force measurement during lift-up

speed of 5000 rpm. To demonstrate the MIMO controller's effectiveness, it is not applied at first. Due to the large I_p to I_r ratio, the gyroscopic effect is very significant, and it caused the system to become unstable. The large vibrations in the $\theta_x - \theta_y$ plane, which grows exponentially, are illustrated in Figs. 15 and 16. As depicted in Fig. 17, the gyroscopic effects also caused significant amplifier voltage saturations in the tilting control coils. The SISO controller finally failed to compensate the tilt motion and become saturated. Notice that the catcher bearing system is not included in the model. Therefore, the tilt motion continues to grow without boundary (Fig. 18). In practice, the rotor will delevitate and converge to a limit cycle bounded by the catcher bearings.

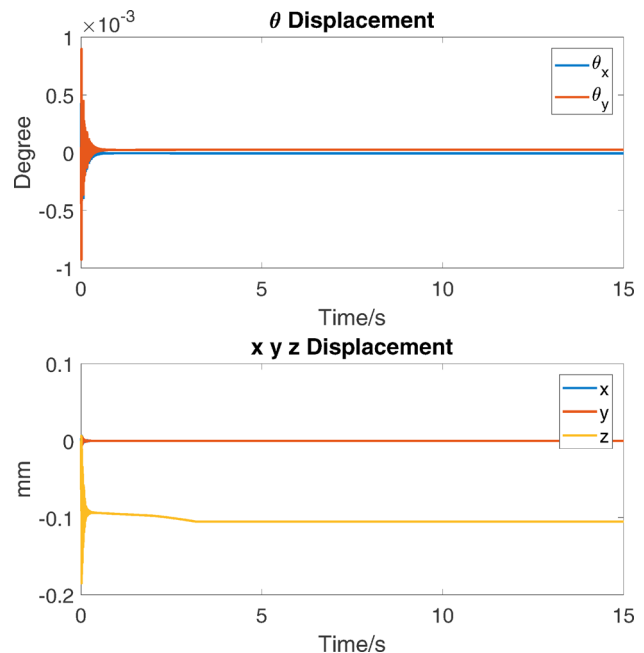


Fig. 14 Stator vibrations during lift-up

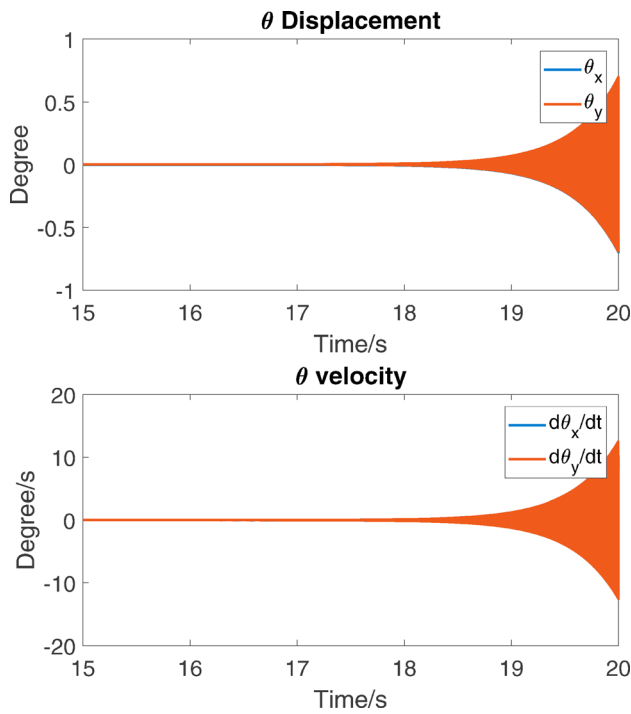


Fig. 15 Full-speed flywheel attitudes under gyroscopic and sensor runout effects (without MIMO control)

5.3 Multi-Input–Multi-Output Controlled High-Speed Flywheel Operation. With the MIMO controller applied, the flywheel is stabilized at 5000 rpm. The amplifiers outputs for radial actuators oscillate in the range of less than 5v pk–pk. The remaining amplifiers will oscillate around 10v pk–pk. At least two

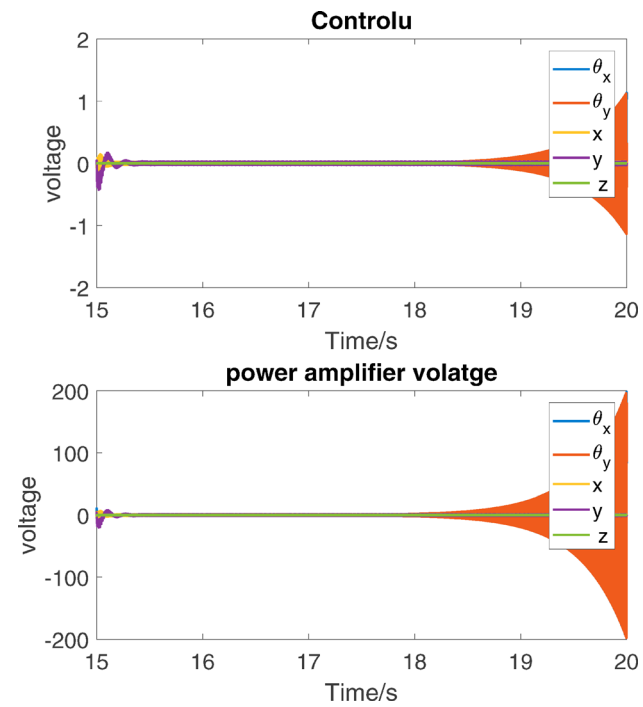


Fig. 17 Full-speed flywheel controller and power amplifier (without MIMO control)

notches are needed to deal with the runout effects, which will likely cause excessive burden on the power amplifiers and delevitate the rotor if without given any mitigation. Imbalance forces are much less harmful than run-out because that they occur at a lower frequency and only affect the radial actuator which has less inductance burden (Figs. 19–22).

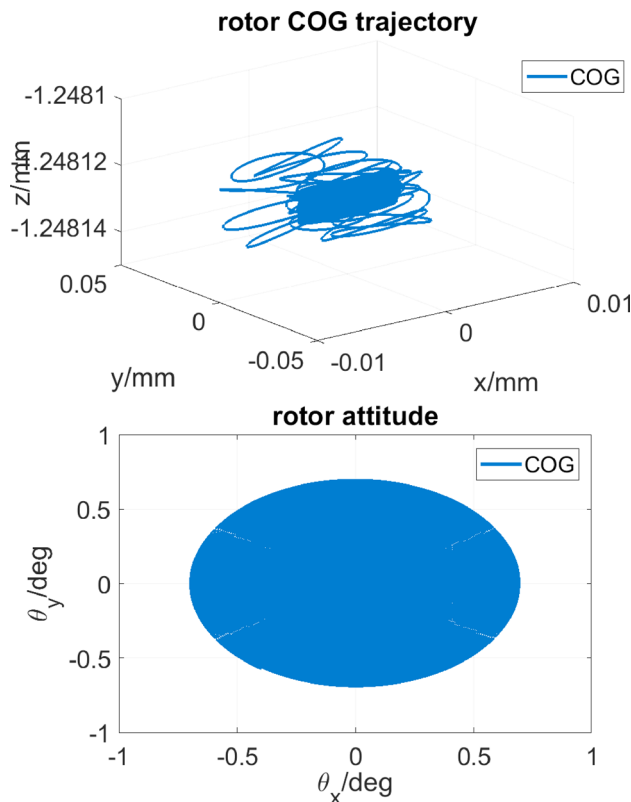


Fig. 16 Full-speed flywheel trajectory under gyroscopic and sensor runout effects (without MIMO control)

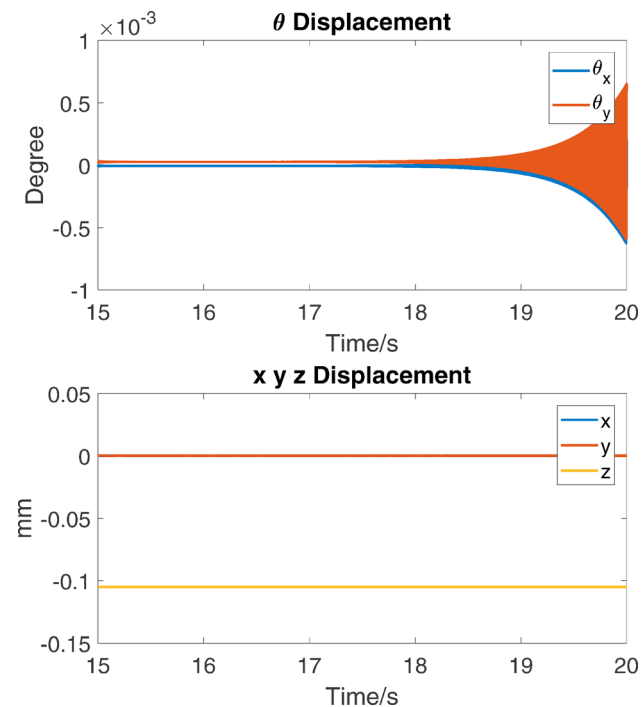


Fig. 18 Full-speed stator attitude vibrations (without MIMO control)

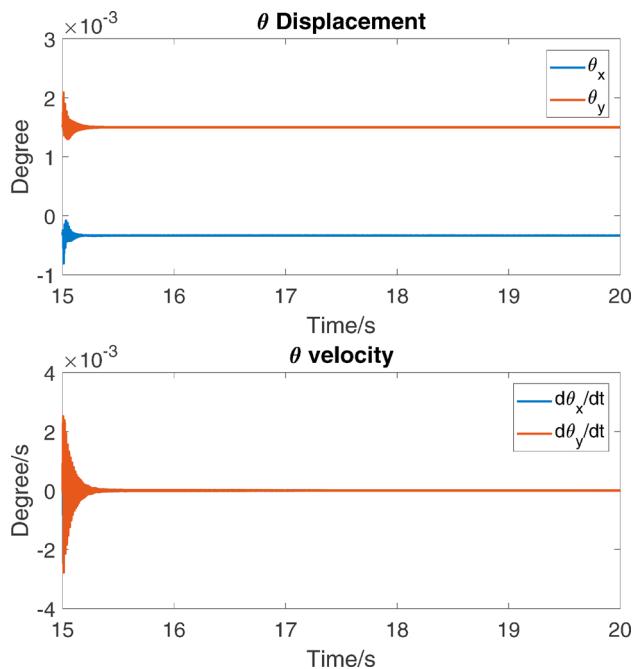


Fig. 19 Full-speed flywheel attitudes under gyroscopic and sensor runout effects (with MIMO control)

6 Conclusion

This paper provides a systematic and comprehensive synthesis for dynamical modeling and control of a utility-scale energy storage flywheel. The uniqueness of the flywheel-AMB system includes a rotor with significant gyroscopic effects, a solid-core, combination magnetic bearing, and a flexible supporting structure, which are often omitted in many existing magnetic bearing control schemes. We implement detailed dynamic models for each component of the system based on experimental data. Transient

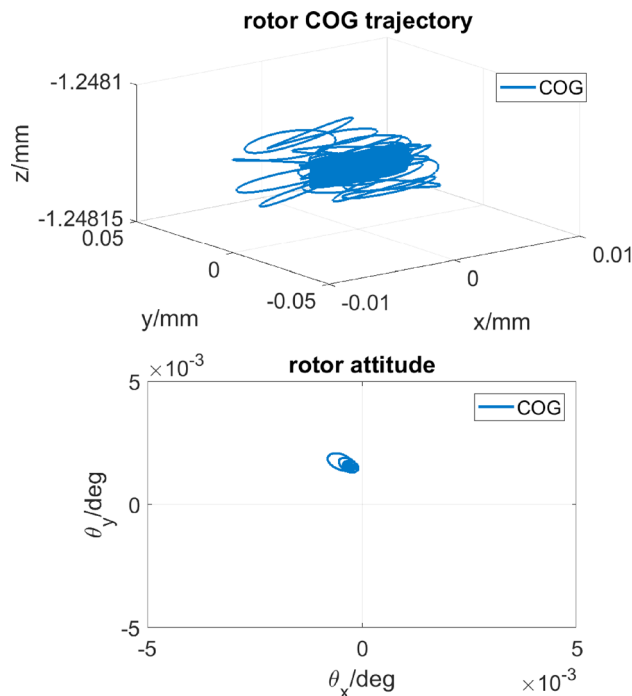


Fig. 20 Full-speed flywheel trajectory under gyroscopic and sensor runout effects (with MIMO control)

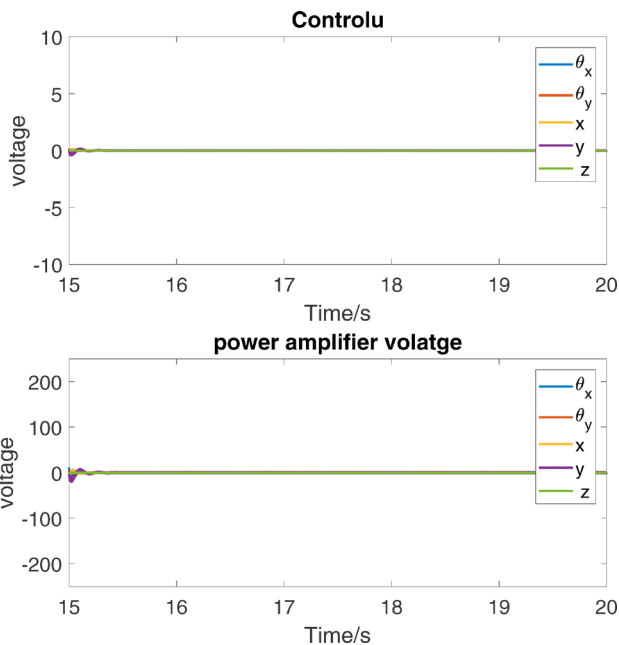


Fig. 21 Full-speed Flywheel control and power amplifier (with MIMO control)

simulations with an initial error of 20% are conducted based on the modeling and control algorithm. Results predict a successful magnetic lift-up for the 5543 kg flywheel. For the flywheel stability and disturbance rejection at full speed, we demonstrate the effectiveness of a MIMO torque canceling control algorithm even with a high ratio of $I_p/I_t \approx 2$. In the case when notch filters are also applied, the coil voltage variations are reduced to less than 10v pk-pk. The flywheel is stabilized to axially vibrations of less than 3.8×10^{-3} mm, radial vibrations between $(-5 \times 10^{-2}, 5 \times 10^{-2})$ mm and tilt vibrations of less than 0.5 m deg.

Future work will focus on improving the current software-based simulation code, which requires parameters and user input

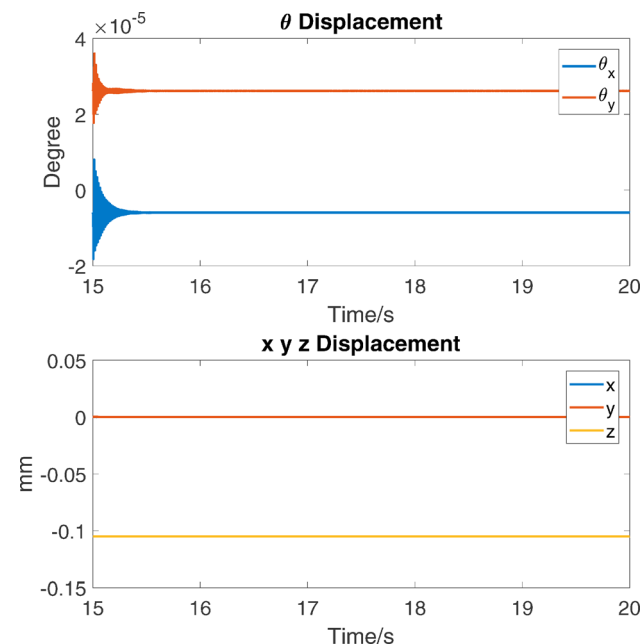


Fig. 22 Full-speed stator attitude vibrations (with MIMO control)

profiles to be predefined. A hardware-in-the-loop simulation in a real-time operating system will ensure that the controller and the plant model running at a time-step closer to its physical model. This allows evaluation of the operational modes for the flywheel system in details before it is tested under high spinning speed. More importantly, a gain schedule scheme is needed to stabilize the flywheel at different speeds over its entire operational range between 5000 rpm and 2500 rpm, and to suppress resonances when it passes through critical speeds.

Acknowledgment

The authors would like to thank Thomas Erwin and Randall Tucker, and many other undergraduate students from Texas A&M University, for their work in this project.

Nomenclature

B_i	= flux density associated with control current
B_{pm}	= flux density associated with permanent magnets
C_s	= damping matrix of the supporting structure
D	= the matrix of the derivative gain
D_f	= transformation matrices of structure-to-AMB magnetic forces
D_s	= transformation matrices of structure-to-AMB sensory signal
E	= energy capacity of the flywheel
G_f	= the matrix of the flywheel rotor gyroscopic
G_{PA}	= the matrix of the PA feedback gain
G_{sn}	= the matrix of the sensory gain
i	= the vector of the PA output current
K	= shape factor
K_i	= current stiffness matrix of the AMB
K_p	= position stiffness matrix of the AMB
K_{PA}	= the matrix of the PA output gain
K_s	= stiffness matrix of the supporting structure
L	= matrix of the coil inductance
L_g	= matrix of the lag compensators
L_l	= matrix of the lead compensators
M_f	= mass/inertia matrix of the flywheel rotor
M_s	= mass/inertia matrix of the supporting structure
N_f	= matrix of the low pass filters
P	= matrix of the proportional gain
q_f	= state variable of the flywheel rotor
q_r	= vector of the runout disturbance
q_s	= state vector of the supporting structure
q_s^c	= state vector of the AMB
R	= matrix of the coil resistance
T_{sn}	= matrix of the sensory filter constant
TF_{if}	= matrix of AMB eddy current effect dynamics
V	= vector of the PA output voltage

ϕ = magnetic flux

μ_0 = the magnetic permeability of free space

References

- [1] Sebastián, R., and Peña Alzola, R., 2012, "Flywheel Energy Storage Systems: Review and Simulation for an Isolated Wind Power System," *Renewable Sustainable Energy Rev.*, **16**(9), pp. 6803–6813.
- [2] Toliyat, H. A., Talebi, S., McMullen, P., Huynh, C., and Filatov, A., 2005, "Advanced High-Speed Flywheel Energy Storage Systems for Pulsed Power Applications," *IEEE Electric Ship Technologies Symposium*, Philadelphia, PA, July 25–27, pp. 379–386.
- [3] Sung, T. H., Lee, J. S., Han, Y. H., Han, S. C., Choi, S. K., and Kim, S. J., 2002, "300 Wh Class Superconductor Flywheel Energy Storage System With a Horizontal Axle," *Phys. C*, **372–376**(Pt. 3), pp. 1451–1456.
- [4] Jinji, S., Ziyang, J., Weitao, H., and Gang, L., 2017, "A Novel Integrated 4-DOF Radial Hybrid Magnetic Bearing for MSCMG," *J. Magn. Magn. Mater.*, **421**, pp. 86–97.
- [5] Park, J., Palazzolo, A., and Beach, R., 2008, "MIMO Active Vibration Control of Magnetically Suspended Flywheels for Satellite IPAC Service," *ASME J. Dyn. Syst., Meas., Control*, **130**(4), p. 041005.
- [6] Lei, S., and Palazzolo, A., 2008, "Control of Flexible Rotor Systems With Active Magnetic Bearings," *J. Sound Vib.*, **314**(1–2), pp. 19–38.
- [7] Tang, E., Fang, J., Zheng, S., and Jiang, D., 2015, "Active Vibration Control of the Flexible Rotor to Pass the First Bending Critical Speed in High Energy Density Magnetically Suspended Motor," *ASME J. Eng. Gas Turbines Power*, **137**(11), p. 112501.
- [8] Lei, S., Palazzolo, A., Na, U., and Kascak, A., 1999, "Fuzzy Logic Control of Magnetic Bearings for Suppression of Vibration Due to Sudden Imbalance," *Fifth International Symposium of Magnetic Suspension Technology*, Santa Barbara, CA, Dec. 1–3, pp. 459–471.
- [9] Wang, Z., 2011, "A Novel Flywheel and Operation Approach for Energy Recovery," Ph.D. thesis, Texas A&M University, College Station, TX.
- [10] Wang, Z., Palazzolo, A., and Park, J., 2012, "Hybrid Train Power With Diesel Locomotive and Slug Car—Based Flywheels for NOx and Fuel Reduction," *J. Energy Eng.*, **138**(4), pp. 215–236.
- [11] Li, X., Palazzolo, A., McMullen, P., Wang, Z., and Tingey, D., 2015, "Shaft-Less Energy Storage Flywheel," *ASME Paper No. ES2015-49079*.
- [12] Li, X., Anvari, B., Palazzolo, A., Toliyat, H., and Wang, Z., 2017, "A Utility-Scale Flywheel Energy Storage System With a Shaftless, Hubless, High Strength Steel Rotor," *IEEE Trans. Ind. Electron.*, **65**(8), pp. 6667–6675.
- [13] Palazzolo, A. B., Tucker, R., and Wang, Z., 2011, "Shaft-Less Energy Storage Flywheel," U.S. Patent No. **8633625B2**.
- [14] Genta, G., 1985, "Application of Flywheel Energy Storage Systems," *Kinetic Energy Storage*, Elsevier, New York, pp. 27–46.
- [15] Anvari, B., Li, X., Toliyat, H. A., Palazzolo, A., Wang, Z., and Han, X., 2017, "A Coreless Permanent-Magnet Machine for a Magnetically Levitated Shaft-Less Flywheel," *IEEE International Electric Machines and Drives Conference (IEMDC)*, Miami, FL, May 21–24, pp. 1–7.
- [16] McMullen, P. T., Huynh, C. S., and Hayes, R. J., 2000, "Combination Radial-Axial Magnetic Bearing," *Seventh International Symposium on Magnetic Bearings*, Zurich, Switzerland, Aug. 23–25, pp. 473–478.
- [17] Bjorn, G., and Semlyen, A., 1999, "Rational Approximation of Frequency Domain Responses by Vector Fitting," *Power Delivery, IEEE Trans.*, **14**(3), pp. 1052–1061.
- [18] Chiesa, N., and Gustavsen, B., 2014, "Frequency-Dependent Modeling of Transformer Winding Impedance From R/L Measurements," *IEEE Trans. Power Delivery*, **29**(3), pp. 1511–1513.
- [19] Okada, Y., Nagai, B., Shimane, T., and Bearing, T. M., 1992, "Cross-Feedback Stabilization of the Digitally Controlled Magnetic Bearing," *ASME J. Vib. Acoust.*, **114**(1), pp. 54–59.
- [20] Ahrens, M., Kucera, L., and Larssonneur, R., 1996, "Performance of a Magnetically Suspended Flywheel Energy Storage Device," *IEEE Trans. Control Syst. Technol.*, **4**(5), pp. 494–502.